CONF-9610207--1
ANL/ET/CP--91499

MODELING OF EDDY CURRENT PROBE RESPONSE FOR STEAM GENERATOR TUBES*

by

S. Bakhtiari and D. S. Kupperman

Energy Technology Division
Argonne National Laboratory
Argonne, Illinois 60439

To be presented at the 24th Water Reactor Safety Information Meeting, Bethesda, MD, October 21-23, 1996

*Work supported by Office of Nuclear Regulatory Research, U. S. Nuclear Regulatory Commission under Contract W-31-109-ENG-38

DISCLAIMER

Modeling of Eddy Current Probe Response for Steam Generator Tubes

S. Bakhtiari and D. S. Kupperman
Energy Technology Division
Argonne National Laboratory

Abstract - Sample calculations were performed with a three-dimensional (3-D) finite-element model analysis that describe the response of an eddy current (EC) probe to steam generator (SG) tubing artifacts. Such calculations could be very helpful in understanding and interpreting of EC probe response to complex tube/defect geometries associated with the inservice inspection (ISI) of steam generator (SG) tubing. The governing field equations are in terms of coupled magnetic vector and electric scalar potentials in conducting media and of total or reduced scalar potentials in nonconducting regions. To establish the validity of the model, comparisons of the theoretical and experimental responses of an absolute bobbin probe are given for two types of calibration standard defects. Preliminary results are also presented from a recent theoretical study of the effect of ligament size in axial cracks on EC indications with conventional ISI bobbin probes.

INTRODUCTION

Eddy current nondestructive testing (NDT) techniques are currently the primary method for ISI of SG tubing. EC inspection is routinely carried out with bobbin coil probes that are very rapid compared with most other techniques Because of technological advancements in digital electronics, real-time data acquisition and analysis, and probe design, EC inspection techniques provide increased resolution and sensitivity. However, interpretation of these signals is often difficult even for experienced operators. A better understanding of the nature of the interaction of the induction coil field with heterogeneous media can lead to improved analysis and interpretation of EC NDT results. Exact solutions using analytical techniques,[1,2] as well as two-dimensional numerical solutions,[3] are limited to relatively idealized probe/defect geometries. More flexible computational techniques such as the finite-element method (FEM) are required for the analysis of more realistic probe/defect geometries. The results from such calculations can help in development of appropriate characterization schemes and can reduce the need for expensive experimental work. Further, such models may also be used to develop a data base of simulated defect indications that can be used for initial characterization of improved signal processing and real-time data analysis techniques.

Probe responses to typical calibration standard tubing artifacts were calculated with a 3-D FEM-based code ELEKTRA by Vector Fields. The governing electromagnetic (EM) field equations in terms of magnetic vector and electric scalar potentials in conducting media and reduced or total scalar potentials in nonconducting regions are solved using finite-element discretization. Probe impedance is determined through energy and power calculations. The signal trajectory in the impedance plane, due to probe motion, is determined by calculating the response at discrete points along the tube axis. Representative test cases that simulate steady-state solutions using both differential and absolute bobbin coils are presented here. Preliminary results of a recent study of the effect of ligament size in axial cracks on the EC signals from conventional bobbin coil probes are also presented.

EM FORMULATION

The governing field equations used in the 3-D FEM problem space are given next. In the conducting regions, these equations are expressed in terms of the magnetic vector potential $\overline{A}$ and electric scalar potential V. In nonconducting regions, they are expressed in terms of either total (ψ) or reduced (ϕ) scalar potentials. Application of the Coulomb or Lorentz gauge, respectively, would allow simultaneous solution of coupled or decoupled vector and scalar potential equations. In conducting media, where the induced eddy currents flow, the governing equations can be written as[4]

$$\nabla \times \frac{1}{\mu} \nabla \times \overline{A} - \nabla \frac{1}{\mu} \nabla \cdot \overline{A} + \sigma \frac{\partial \overline{A}}{\partial t} + \sigma \nabla V = 0 \tag{1}$$

$$\nabla \cdot \sigma \nabla V + \nabla \cdot \sigma \frac{\partial \overline{A}}{\partial t} = 0 \tag{2}$$

and in nonconducting regions that contain the impressed current sources, the scalar potential equations are defined as

$$\nabla \cdot \mu \nabla \phi - \nabla \cdot \mu \left(\int_{\Omega} \frac{\overline{J} \times \overline{R}}{|\overline{R}|^3} d\Omega \right) = 0 \tag{3}$$

$$\nabla \cdot \mu \nabla \psi = 0, \tag{4}$$

which are then solved using finite-element discretization. The intrinsic electrical properties of each medium are incorporated through permeability μ and conductivity σ. The quantities of interest for EC NDT, namely, the change in the coil resistance and reactance, for impedance probes can be determined through energy and power calculations by using

$$W = \frac{1}{2} \int_{v} \overline{B} \cdot \overline{H} \, dv \tag{5}$$

$$P = \int_{v} \frac{J^2}{\sigma} dv \tag{6}$$

The computer-aided-design-based preprocessor stage of the software allows generation and discretization of the finite-element mesh containing the model geometry. Analysis and display of the solutions are carried out at the postprocessing stage.

NUMERICAL AND EXPERIMENTAL RESULTS

A series of test case simulations were initially carried out to verify the accuracy of the FEM solutions by comparison with detailed experimental measurements. The experimental EC data, supplied by C. V. Dodd,[†] were made on a large aluminum tube containing through-wall holes and axial slits. Measurements were made at three different frequencies with a Hewlett-Packard impedance analyzer and a specially constructed absolute bobbin coil (SN480A). The results presented here compare the experimental data for a through-wall hole and an axial slit with the FEM calculations. The results are expressed in terms of both calculated impedance variations as a function of probe position inside the tube and impedance-plane plots that simulate conventional EC instrument display.

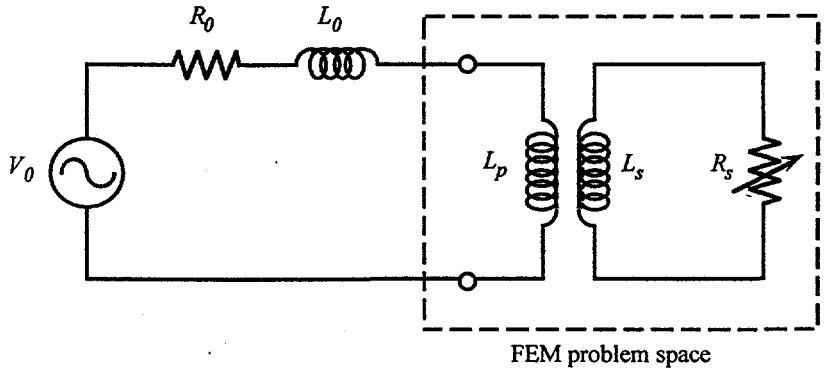

Fig. 1. Lumped element equivalent circuit of EC probe and sample with the region of problem space modeled by FEM shown within the dashed rectangle.

Figure 1 shows the lumped element equivalent circuit for the probe and test sample (tube) interaction modeled as primary and secondary sides of a transformer circuit. Also shown within the dashed rectangle is the part of the circuit modeled by the FEM problem space. In reference to this figure, it should be noted that the final solutions are normalized to eliminate explicit dependence of the parameters on the coil/cable resistance R_0. These normalized parameters are experimentally determined as

$$X_n = \frac{X}{X_0} \tag{7}$$

$$R_n = \frac{R - R_0}{X_0}, \tag{8}$$

[†]Experimental results provided by C. V. Dodd were completed while with Oak Ridge National Laboratory.

where

$$X_0 = \omega L_0 \tag{9}$$

represents the coil reactance in air. By using the normalized variables (equations 7 and 8), R_0 can be ignored. This normalization allows direct comparison of the theoretical and experimental data.

VERIFICATION OF COMPUTATIONAL RESULTS

Figure 2 depicts the aluminum tube standard used in the measurement. It contains three sets of four axially symmetric (repeated every 90° around the tube circumference) artifacts. EC probe readings are the average of nine measurements, each made with a different circumferential orientation. The values of resistance and reactance (in ohms) were determined with a Hewlett-Packard impedance analyzer. In reference to Fig. 3, which shows the cross section of the tube and coil geometry, the tube has inner radius $r_i^t = 38.86$ mm ($\approx$ 1.53 in.) and outer radius $r_o^t = 44.45$ mm ($\approx$ 1.75 in). The through-wall hole artifact has a diameter of $D^h = 11.18$ mm ($\approx$ 0.44 in.), and the slit has a length of $l^g = 36.0$ mm ($\approx$ 1.42 in.) and a width of $w^g = 0.38$ mm ($\approx$ 0.015 in.). The coil has inner radius $r_i^c = 31.75$ mm, outer radius $r_o^c = 38.0$ mm, width $w = r_o^c - r_i^c = 6.25$ mm, and length $l = 6.60$ mm. A measured resistivity value of $\rho = 3.88\,\mu\Omega - cm$ was used to simulate the aluminum tube material. The coil was wound over a Teflon form with #36 gauge wire.

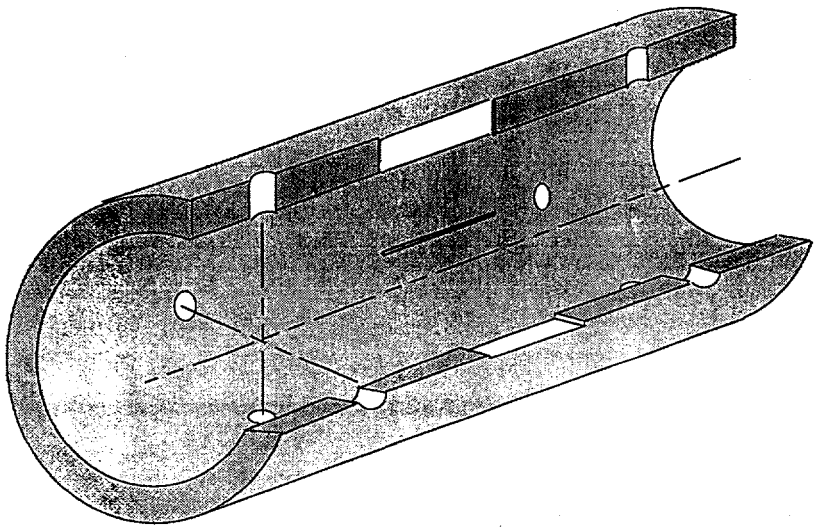

Fig. 2. Geometry of the aluminum tube standard with through-wall hole and axial slit artifacts placed symmetrically (90° apart) around the circumference.

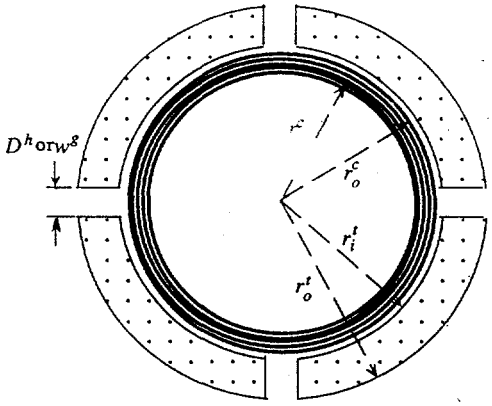

Fig. 3. Cross-sectional geometry of the absolute bobbin coil inside the aluminum tube with one set of through-wall artifacts 90° apart around the circumference.

The computed results are given in terms of both current density distribution over the tube surface and calculated impedance components. In the FEM model, all materials were assumed to be nonmagnetic (i.e., relative permeability $\mu_r = 1$). The coil represents $N = 1836$ turns carrying a unit current density (A/mm^2). Figures 4(a) and (b) depict the tube/coil geometry, along with the distribution of the current density, $|\bar{J}|$, at $f = 0.5$ kHz for the two artifacts modeled here. The coil center in these figures coincides with the defect center in the axial direction. Due to the symmetry of the geometry, only 1/8 of the problem was modeled in both cases. Results are displayed for the case that the probe is positioned at $z = 0$ mm (center of the defect is at $z = 0$ mm). The FEM solution for the distribution of current density on the aluminum tube with a through-wall hole having a diameter of 11.18 mm using an absolute bobbin coil operating at $f = 0.5$ kHz is shown in Fig. 4(a). Current distribution for the slit is shown in Fig. 4(b). The distribution on the tube outer surface at 0.5 kHz shows the distortion along the path of circumferentially induced currents due to presence of through-wall artifacts. It can be observed that the lowest test frequency chosen here allows for detection of outer surface artifacts for the highly conducting aluminum material. On the other hand, attenuation at the highest frequency measured, $f = 7.5$ kHz, would allow detection of only near inner-surface artifacts corresponding to the shallow skin depth.

Figures 5 and 6 show theoretical and experimental results for variation of the coil resistance and reactance as a function of the axial position along the tube and the impedance-plane plot of the same data. The results show close agreement between theory and measurement both for the simulated through-wall hole and axial slit. Agreement for the through-wall hole is not as good at the highest frequency. This could be associated with operating the coil near the coil/cable resonance and the effect of inner winding capacitance at higher frequencies for coils with thick gauge wire. Better consistency between the theory and measurement is generally expected at frequencies away from the resonance where probe sensitivity is minimal to such parameters. The

3-D FEM computations correctly predict the variation of the EC bobbin probe signal in the presence of axisymmetric artifacts.

The above results indicate a substantial difference in the EC signal amplitudes associated with the two artifacts modeled here. Bobbin probe signal amplitude alone can not generally be regarded as an absolute indication of the volumetric extent of defects when comparing different flaw geometries. This can be observed from comparison of the probe impedance responses, which are linearly proportional to the probe output voltage, for the two defect geometries modeled here. Although the through-wall hole has a much greater volume than the axial groove, it results in a smaller perturbation of the coil impedance. Eddy currents always flow through the path of least resistance in a conducting medium. The discontinuity (infinite resistance) introduced by the thin but long axial groove forces the currents to take a contour around the defect which in turn gives rise to a larger impedance mismatch for the probe.

THEORETICAL ANALYSIS OF AXIAL GROOVE WITH LIGAMENT

The preliminary results on the effect of ligaments on bobbin coil signals due to axial grooves are presented below. These test cases pertain to simulation of the probe response to axial grooves, 100% and 75% through-wall, on 22.225-mm (0.875 in.) outer diameter (OD) Inconel 600 tubing with a nominal wall thickness of 1.27 mm (0.05 in.) and conductivity of $\rho = 100.0\ \mu\Omega - cm$. The probes modeled are conventional 18.3 mm (0.72 in.) OD differential and absolute bobbin coils, and the simulations used frequencies of f = 100 kHz and f = 400 kHz, typical frequencies used for multifrequency ISI of SG tubing. Once again, the results are given in terms of both current distribution along the tube and computed resistance and reactance values as a function of probe position. Finally, simulation results are presented to show the expected normalized variation in an absolute bobbin probe signal amplitude at two frequencies as a function of ligament size in axial an groove, 100% and 75% through-wall, respectively.

Figure 7 depicts the cross-sectional geometry of an absolute bobbin coil located symmetrically under an axial slit with a ligament. For all test cases considered here, slit length was arbitrarily chosen to be C = 25.4 mm (1 in.), and unless otherwise specified, the ligament length was taken to be L = 0.127 mm (0.005 in.). The width of the slit was also taken to be 0.127 mm. The ligament was positioned symmetrically in the middle of the slit. Coil length and height were taken to be 1.27 and 1.525 mm, respectively. For the differential bobbin probe, the coil spacing was taken to be 1.525 mm.

Figure 8(a) and (b) show the distribution of current density due to presence of a ligament at f = 100 kHz for a differential and absolute bobbin probe, respectively. To simultaneously display the inner and outer distribution of currents, two 45° top and bottom sections of the tube are shown. In Fig. 8(a), the lagging coil of the differentially wound probe is positioned under the defect at z = 1.5 mm. For the results shown in Fig. 8(b), the absolute coil was positioned in the middle of the axial slit at z = 0. Comparison of the current distributions shown in Fig. 8 with

that shown earlier in Fig. 6(b) for the axial groove without ligament clearly reveals that the small ligament creates a path for the circumferentially induced currents to flow across the slit, which consequently results in a reduction of the probe signal amplitude. Similar results are shown in Fig. 9 for a 75% OD through-wall groove with the same size ligament. Observation of these results also show similar trends except that the presence of a thin layer of normal tubing material under the groove causes currents to flow primarily underneath the artifact and again result in reduction of the signal amplitude relative to the case in which the artifact is 100% through-wall.

Figures 10 and 11 are plots of the computed impedance response of the absolute bobbin probe for the slit, with and without the ligament, at f = 100 kHz and f = 400 kHz, respectively. In both cases, presence of the ligament significantly changes the probe signal variation. Impedance plane plots of the differential coil for the same defect geometry are shown in Fig, 12. Figure 13 shows the computed response for the absolute coil at f = 100 kHz, for the 75% OD slit with and without ligament. As expected, the presence of the ligament results in a significantly smaller change in coil response than for the 100% through-wall slit as a result of the presence of ID tubing material under the defect, which forces the currents to flow primarily underneath the OD artifact. Figure 14 shows impedance variations for the same test case geometry and at the same frequencies except that a differential coil was modeled. For the most part, the results show only small changes in the impedance plane trajectory due to the presence of the ligament, relative to the changes for the 100% through-wall slit.

Finally, to examine the effect of ligament size in a long axial groove on the absolute bobbin coil response, a series of computations were carried out by placing the coil symmetrically under the artifact and then varying the ligament length. The geometry of the model was depicted in Fig. 7. Figure 15(a) shows the result of the analysis at frequencies of 100 and 400 kHz for the 100% through-wall slit. Calculated values are displayed as percent change in probe signal amplitude as a function of ligament length. Similar calculations are shown in Fig. 15(b) for the 75% OD through-wall groove. In both cases, the change in bobbin coil signal amplitude variations quickly drops with the increase in ligament length and approaches the abscissa, which represents no defect.

CONCLUSIONS

Computational electromagnetic results pertaining to modeling of EC NDT of tubing artifacts with absolute and differential bobbin probes were determined with a 3-D FEM analysis code. The validity of solutions for axisymmetric defect geometries was initially demonstrated by comparing theoretical results with laboratory-based measurement data made with an impedance analyzer on an aluminum tube standard. Preliminary simulation results were also presented in an attempt to model the effect of narrow ligaments on bobbin coil indications for a thin slit. These results show the applicability of FEM-based solutions for predicting the response of EC probes to flaws in steam generator tubes, and they also suggest that computational EM models may be helpful for the analysis and interpretation of EC NDT indications.

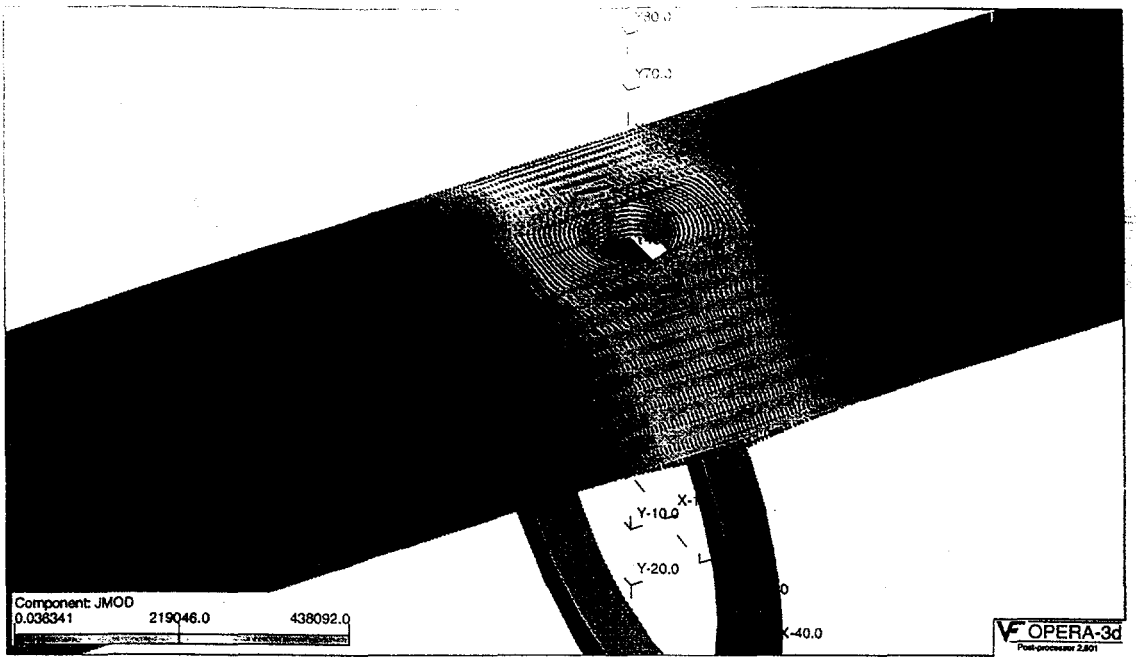

(a)

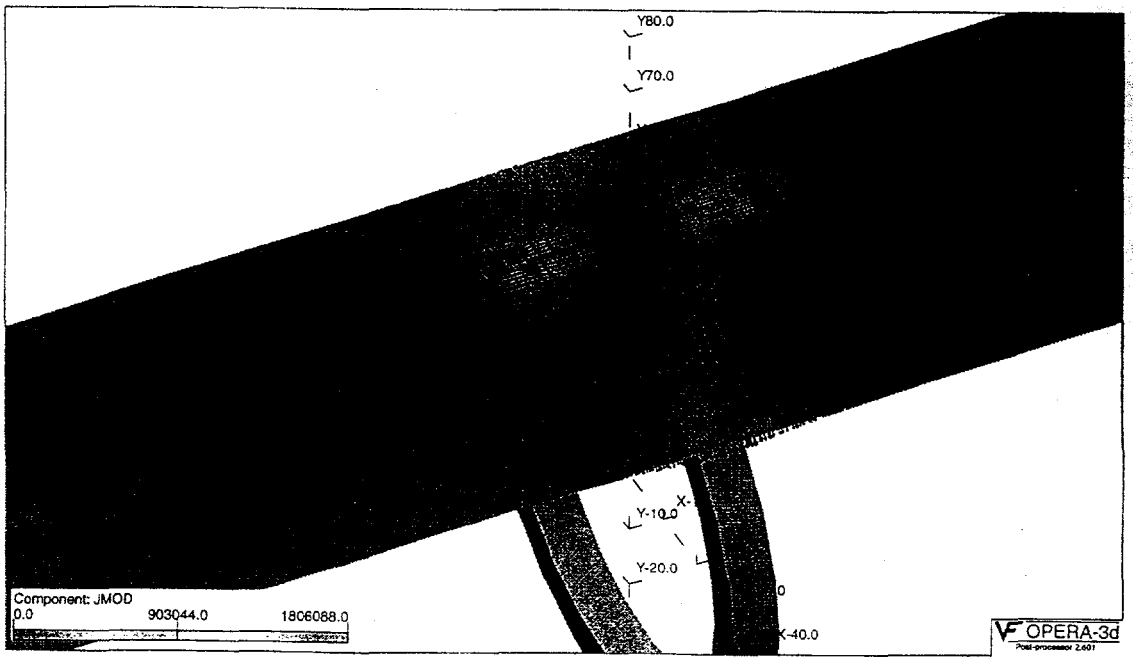

(b)

Fig. 4. FEM solution for the distribution of current density due to an absolute bobbin coil at $f = 0.5$ kHz on the aluminum tube with (a) through-wall hole, and (b) axial slit.

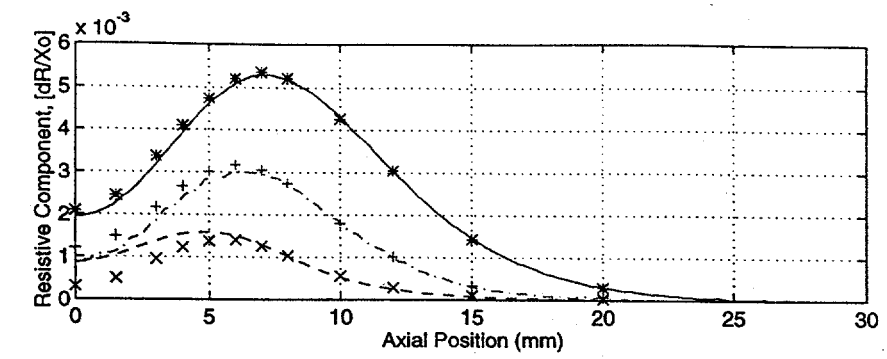

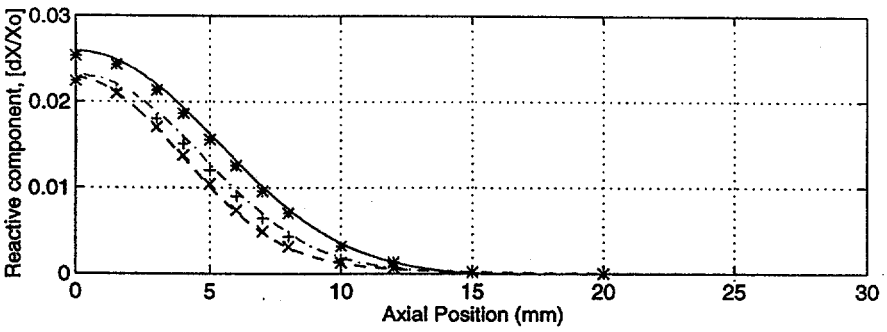

(a)

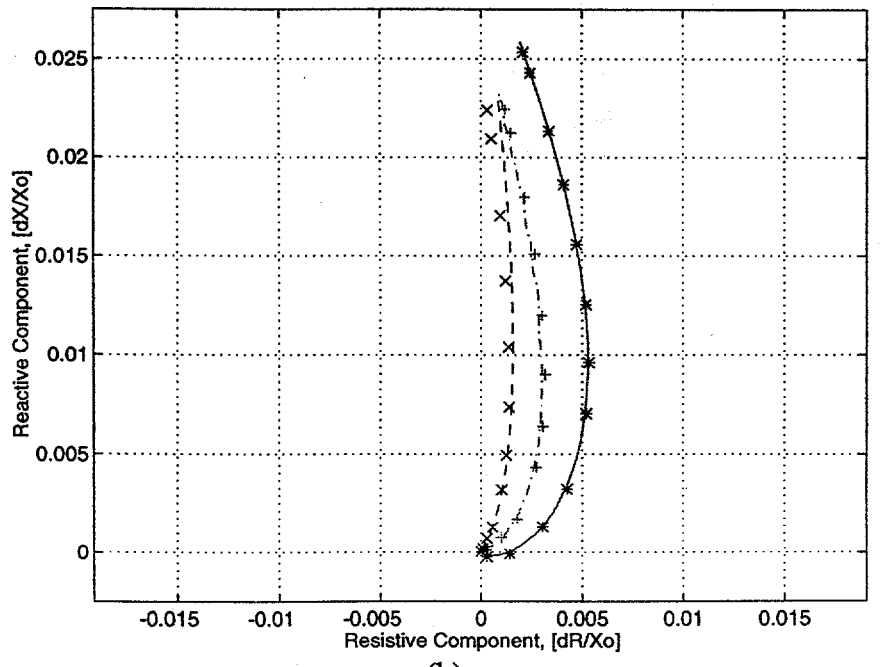

(b)

Fig. 5 Experimental [-, -., --] and numerical [*, +, x] results of (a) resistance and reactance as a function of position of absolute bobbin coil, and (b) impedance-plane signal trajectory, at f = 0.5, 1.2, and 7.5 kHz, respectively. Artifacts are four axially symmetric through-wall holes (90° apart around tube circumference).

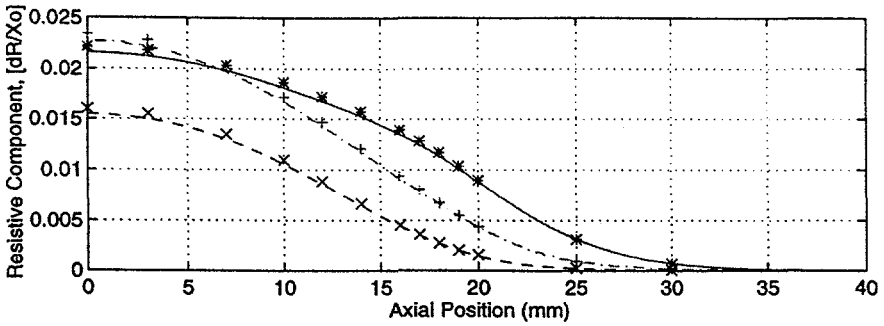

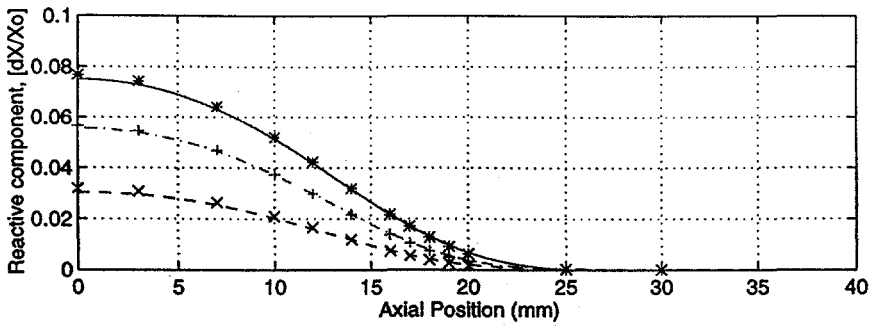

(a)

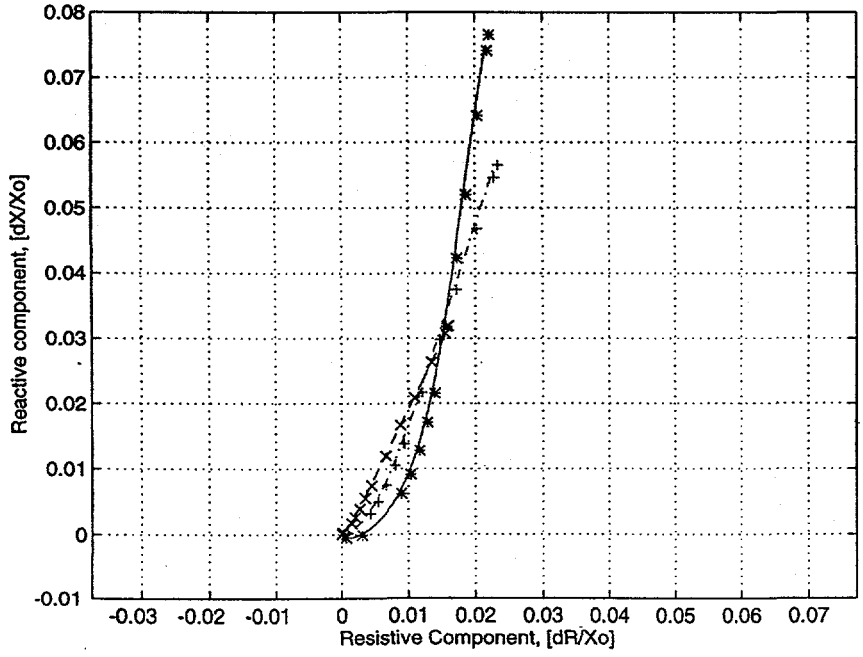

(b)

Fig. 6 Experimental [-, -., --] and numerical [*, +, x] results of (a) resistance and reactance as a function of position of absolute bobbin coil, and (b) impedance-plane signal trajectory, at f= 0.5, 1.2, and 7.5 kHz, respectively. Artifacts are four axially symmetric slits (90° apart around the tube's circumference).

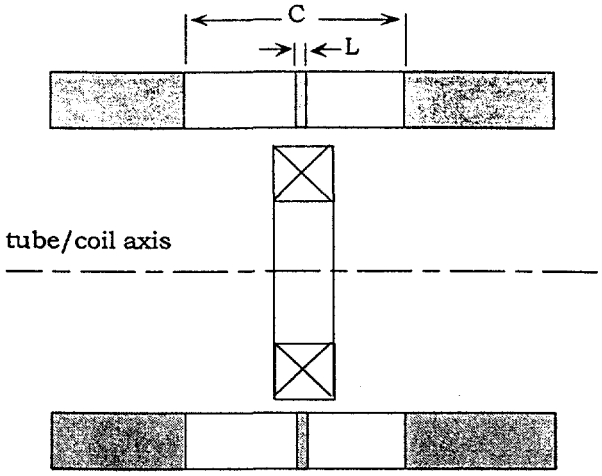

Fig. 7. Cross-sectional geometry of absolute bobbin coil inside a tube with four symmetric axial slits of length C and ligament of length L.

ACKNOWLEDGMENTS

This work was supported by the Office of Nuclear Regulatory Research, U. S. Nuclear Regulatory Commission; Program manager, Dr. Joseph Muscara, Division of Engineering Technology. The authors thank C. V. Dodd for providing the experimental data.

REFERENCES

[1] Pate, J. R., and C. V. Dodd, "Computer Programs for Eddy-Current Defect Studies", Oak Ridge National Laboratory, 1990, NUREG/CR-5553.

[2] C. V. Dodd, "The Use of Computer-Modeling for Eddy-Current Testing," Research Techniques in Nondestructive Testing, ed. R. S. Sharpe, Vol. 3, Ch. 13, pp. 429-479, Academic Press, London, 1977.

[3] Lord, W., and R. Palanisamy, "Development of Theoretical Models for Nondestructive Testing Eddy-Current Phenomena," Eddy-Current Characterization of Materials and Structures, eds. by G. Birnbaum and G. Free, pp 5-21, ASTM, 1981.

[4] Trowbridge, C. W., "An Introduction to Computer Aided Electromagnetic Analysis," Vector Fields Ltd., 1990.

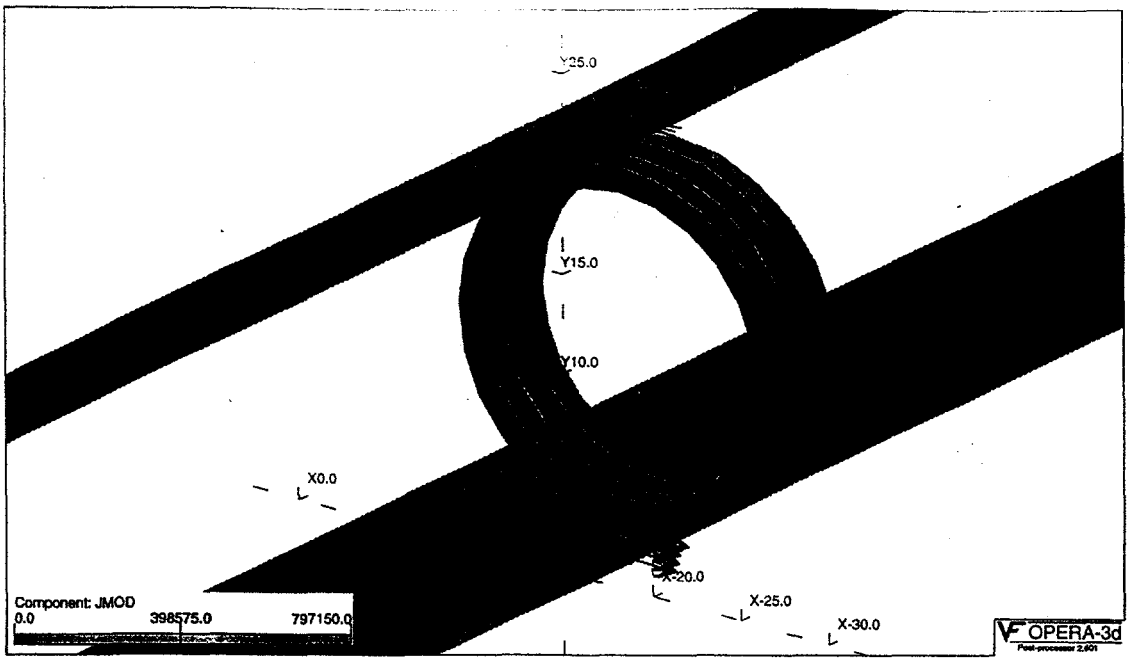

(a)

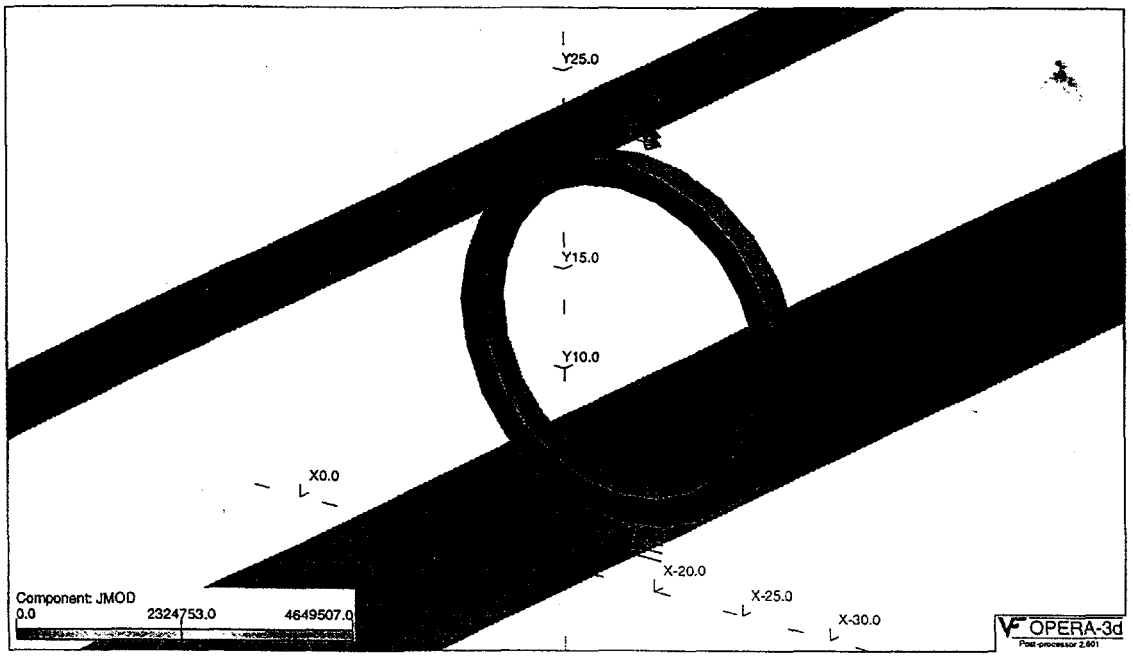

(b)

Fig. 8. FEM solution for distribution of current density due to (a) differential and (b) absolute bobbin coil at $f = 100$ kHz on Inconel 600 tube with 25.4-mm-long, 0.127-mm-wide axial 100% through-wall slit with 0.127-mm long ligament in center.

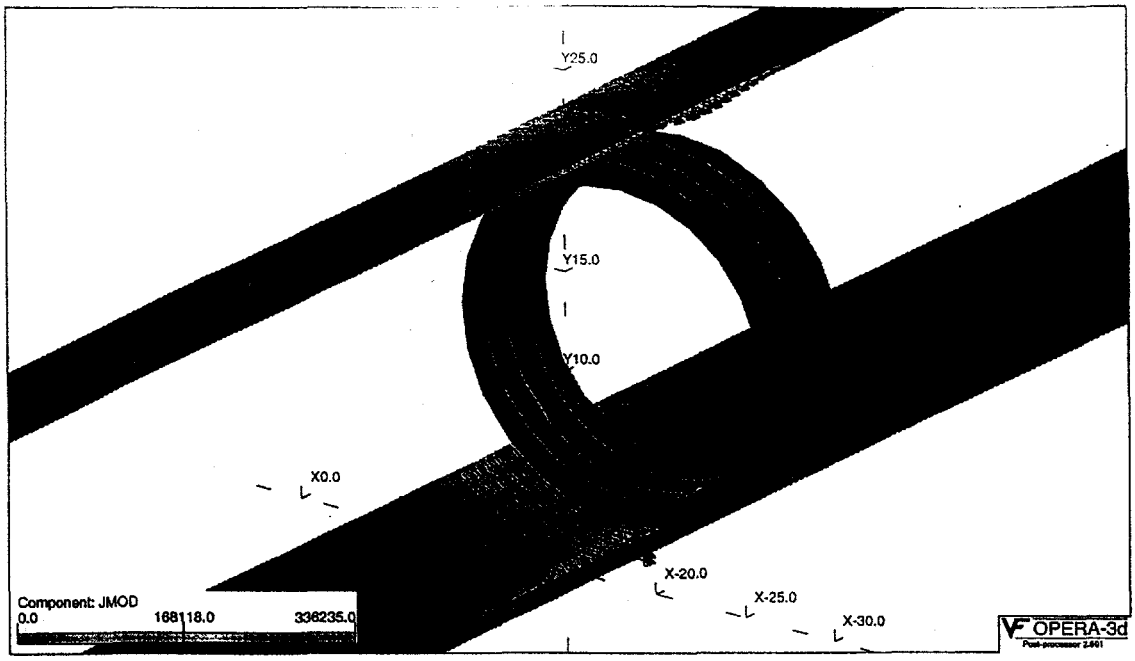

(a)

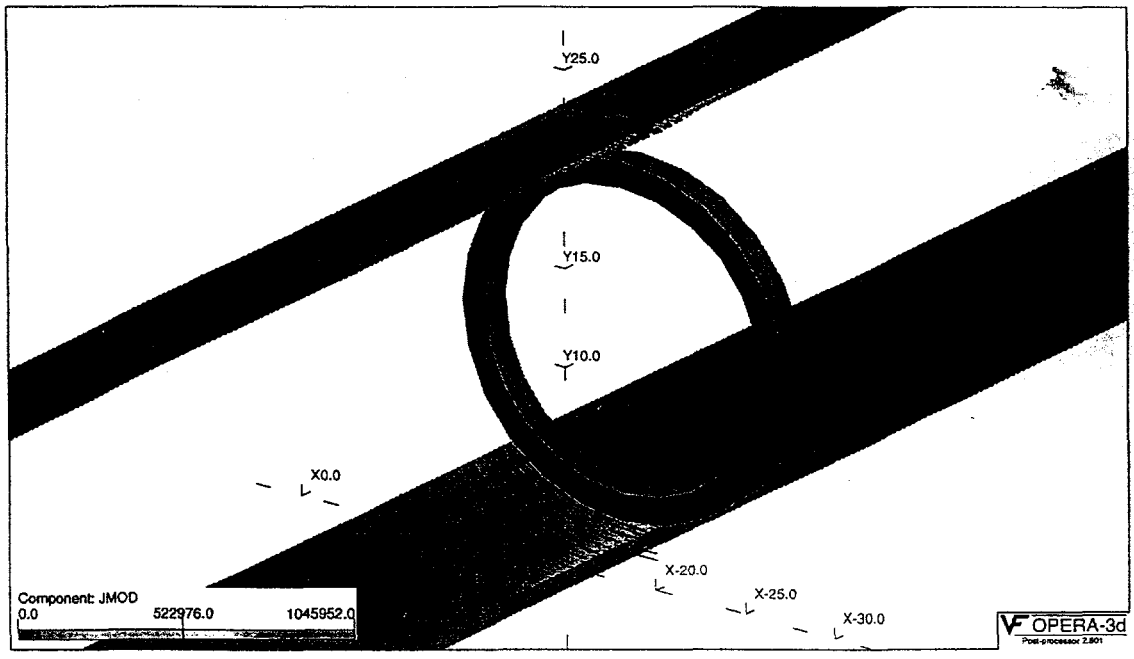

(b)

Fig. 9. FEM solution for distribution of current density due to (a) differential and (b) absolute bobbin coil at $f = 100$ kHz on Inconel 600 tube with 25.4-mm-long, 0.127-mm-wide 75% OD axial groove with 0.127-mm long ligament in center..

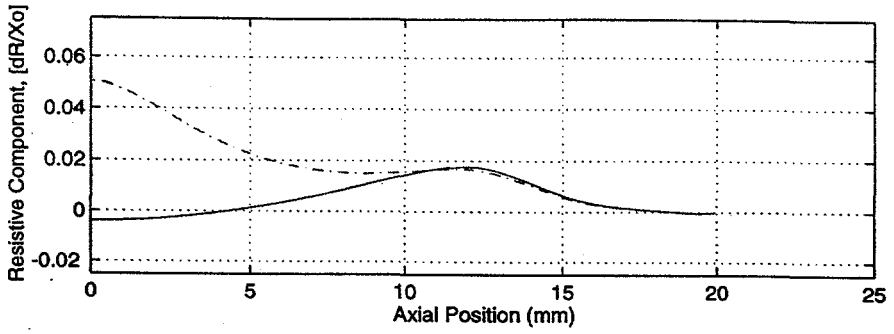

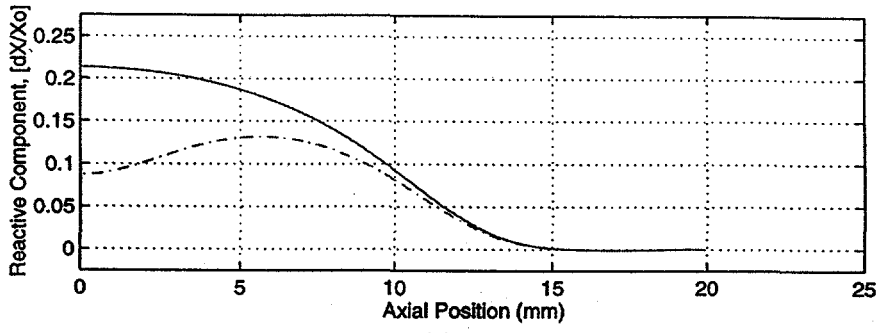

(a)

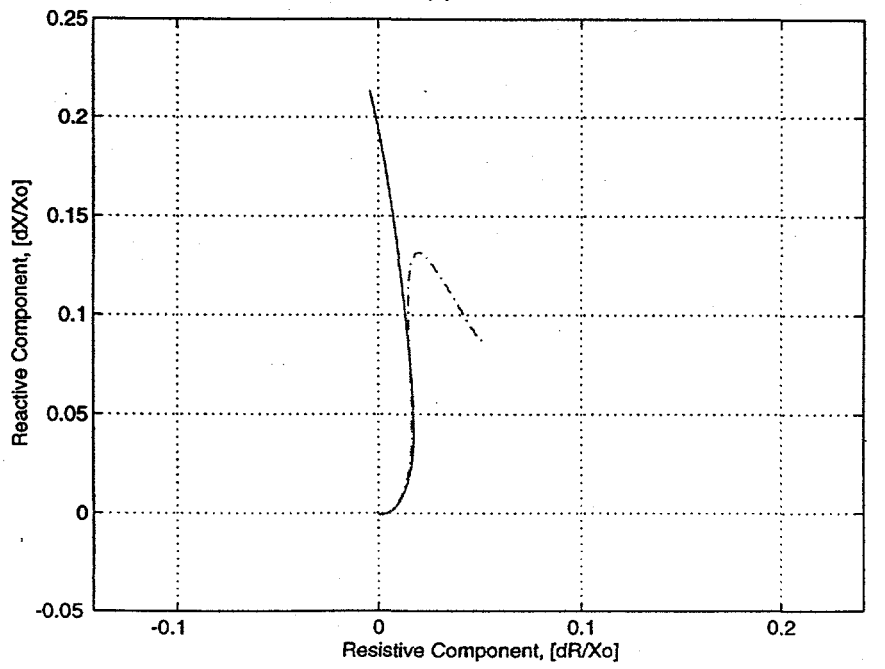

(b)

Fig. 10. Numerical results of (a) resistance and reactance as a function of position, and (b) impedance-plane signal trajectory, at $f = 100$ kHz. Artifacts are four axially symmetric 100% through-wall slits, without (solid line) and with (dashed line) ligament.

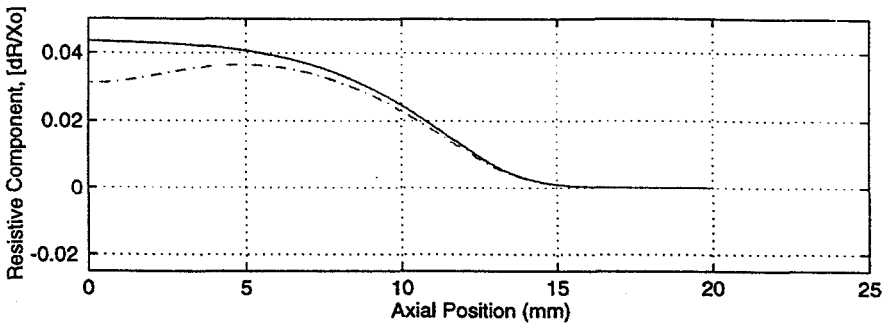

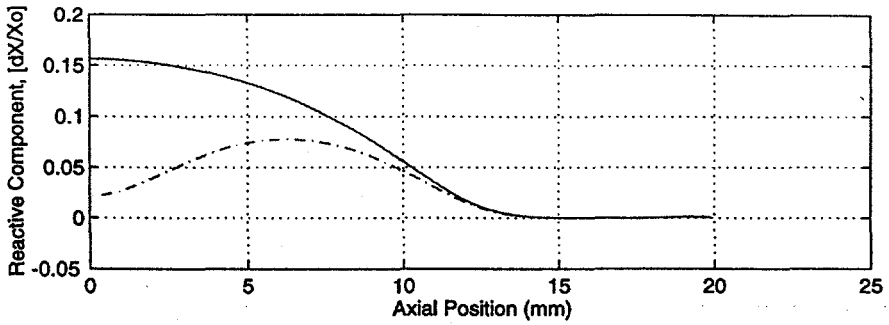

(a)

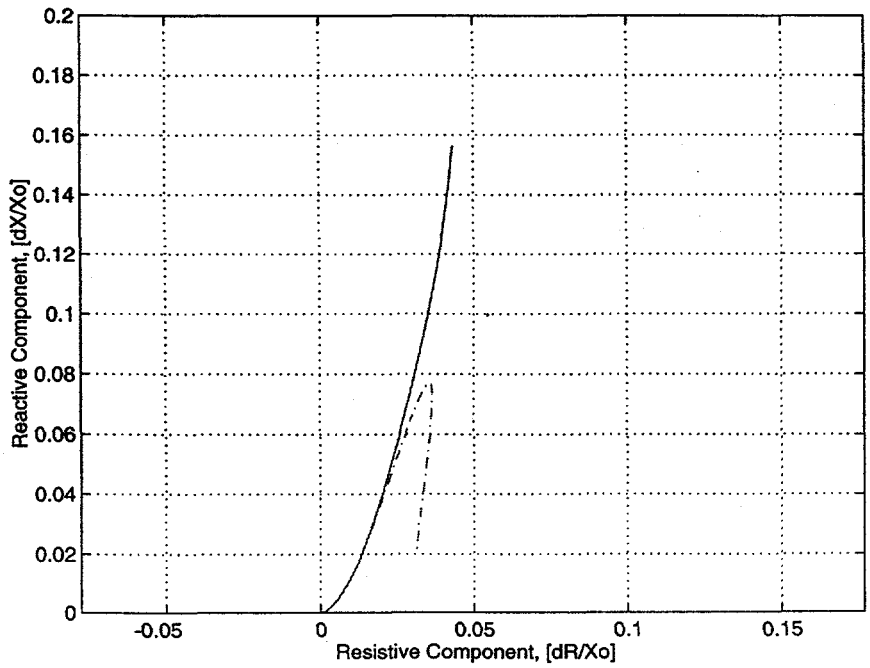

(b)

Fig. 11. Numerical results of (a) resistance and reactance as a function of position, and (b) impedance-plane signal trajectory, at $f = 400$ kHz. Artifacts are four axially symmetric 100% through-wall slits, without (solid line) and with (dashed line) ligament.

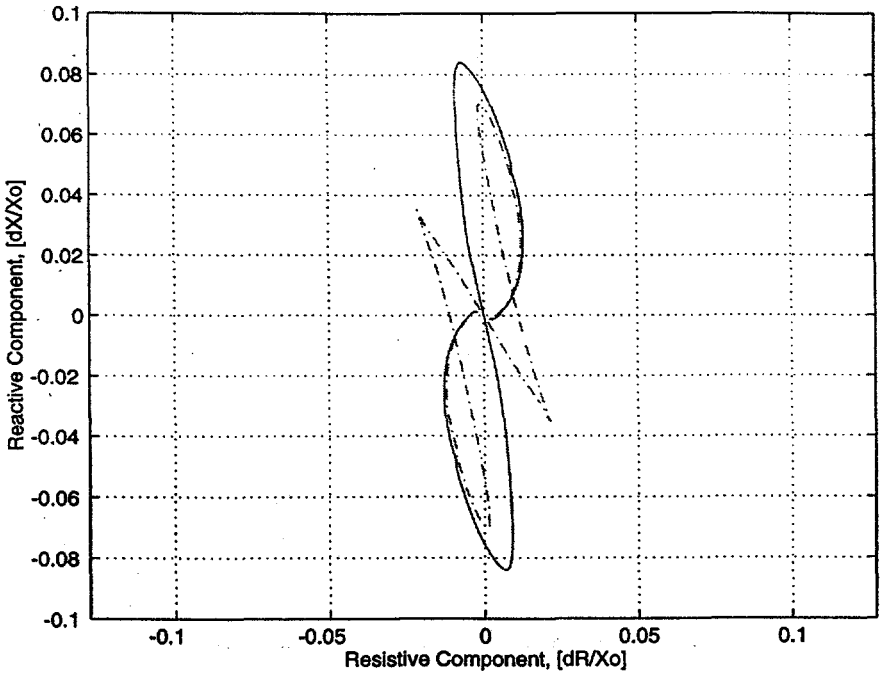

(a)

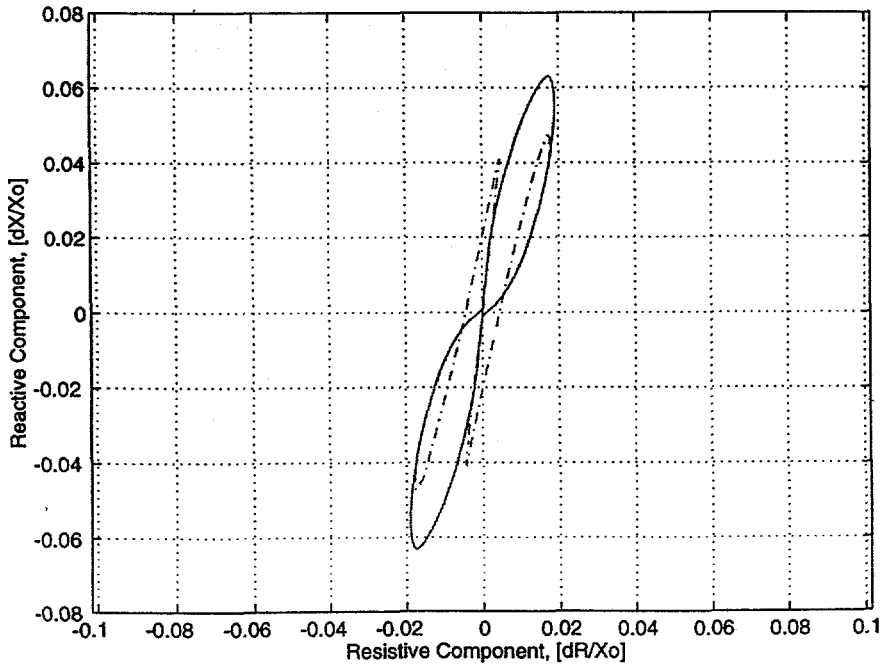

(b)

Fig. 12. Numerical results of impedance-plane signal trajectory, at (a) f = 100 kHz, and (b) f = 400 kHz. Artifacts are four axially symmetric 100% through-wall slits without (solid line) and with (dashed line) ligament.

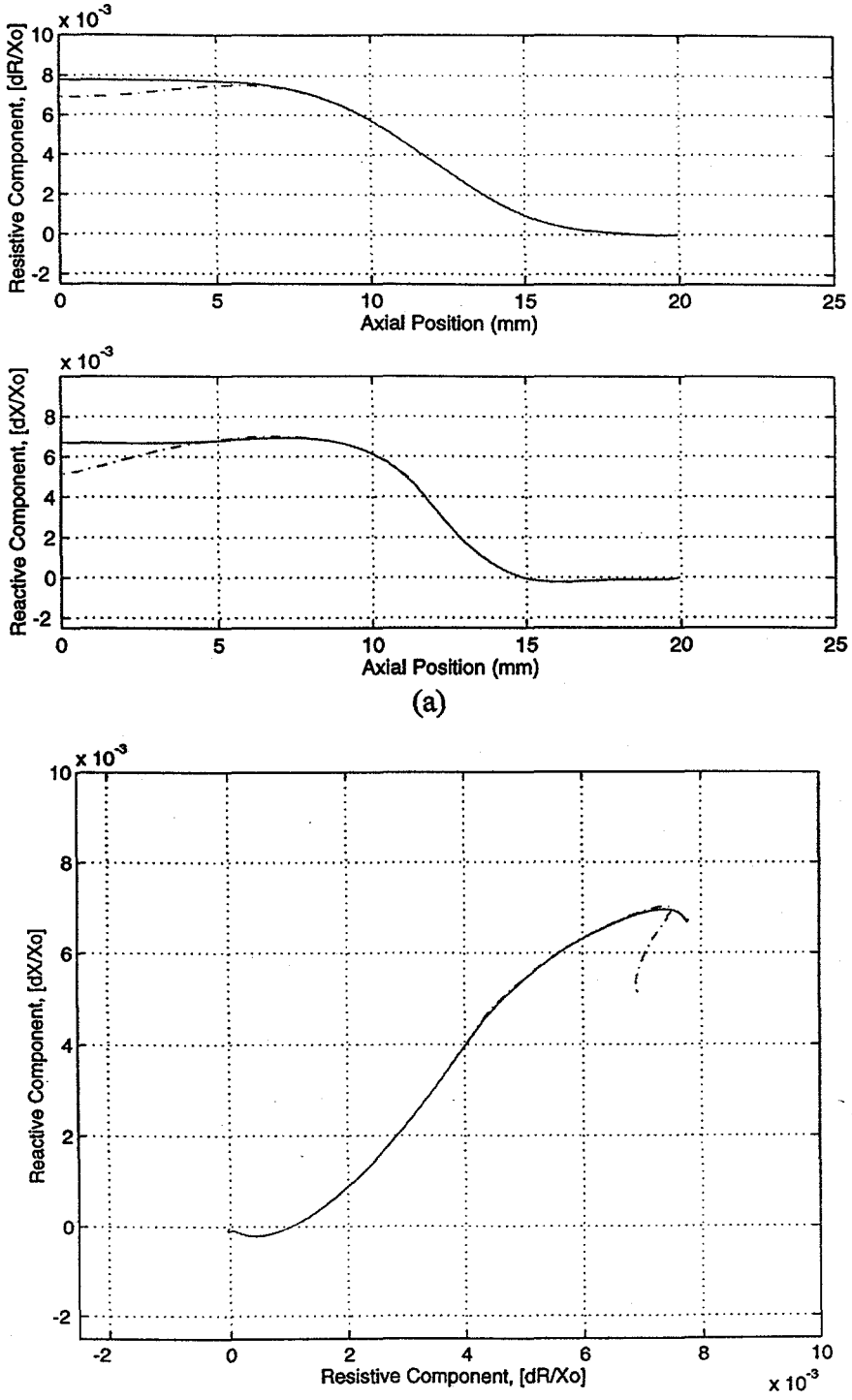

Fig. 13. Numerical results of impedance-plane signal trajectory for absolute bobbin coil, at (a) f = 100 kHz, and (b) f = 400 kHz. Artifacts are four axially symmetric 75% OD grooves without (solid line) and with (dashed line) ligament.

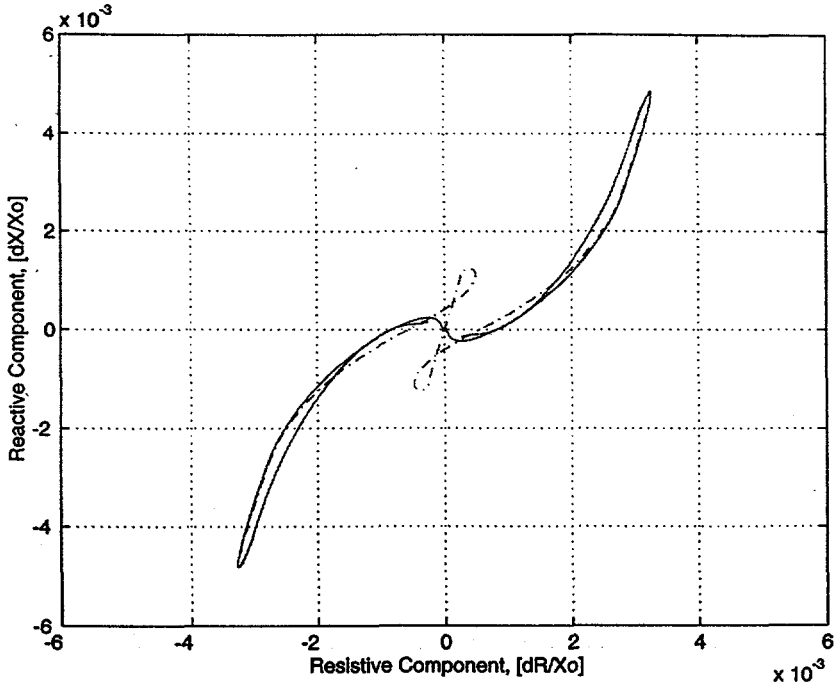

(a)

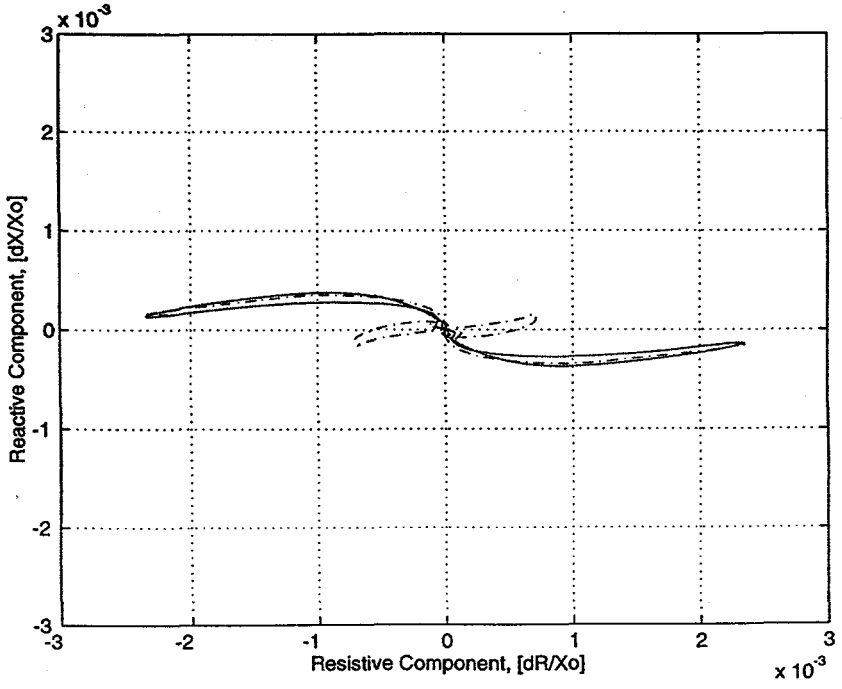

(b)

Fig. 14. Numerical results of impedance-plane signal trajectory for differential bobbin coil, at (a) f = 100 kHz, and (b) f = 400 kHz. Artifacts are four axially symmetric 75% OD grooves without (solid line) and with (dashed line) ligament.

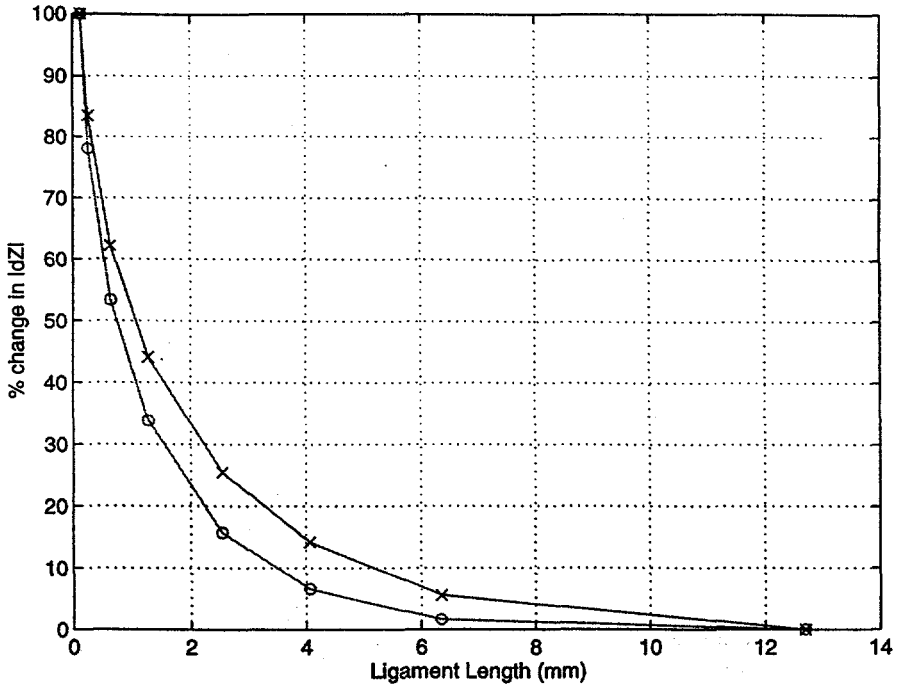

(a)

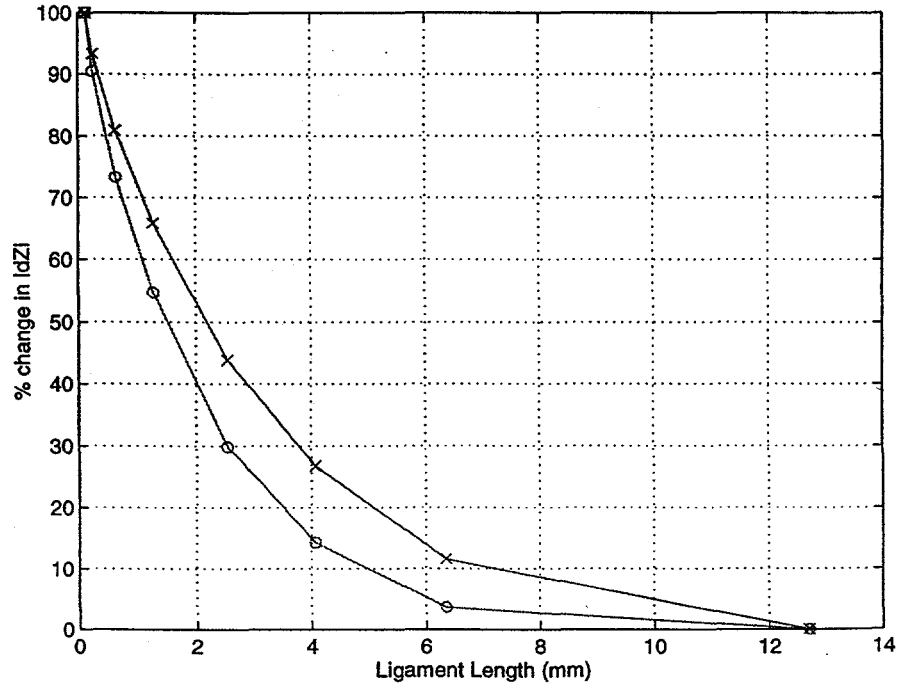

(b)

Fig. (15). Plot of change in absolute probe signal amplitude as a function of ligament length at f = 100 and 400 kHz for (a) 100% through-wall, and (b) 75% OD axial groove.